WASP-44b, WASP-45b and WASP-46b: three short-period, transiting extrasolar planets

D. R. Anderson,[1]* A. Collier Cameron,[2] M. Gillon,[3] C. Hellier,[1] E. Jehin,[3] M. Lendl,[4]
P. F. L. Maxted,[1] D. Queloz,[4] B. Smalley,[1] A. M. S. Smith,[1] A. H. M. J. Triaud,[4]
R. G. West,[5] F. Pepe,[4] D. Pollacco,[6] D. Ségransan,[4] I. Todd[6] and S. Udry[4]

[1] *Astrophysics Group, Keele University, Staffordshire ST5 5BG, UK*
[2] *SUPA, School of Physics and Astronomy, University of St. Andrews, North Haugh, Fife, KY16 9SS, UK*
[3] *Institut d'Astrophysique et de Géophysique, Université de Liège, Allée du 6 Août, 17, Bat. B5C, Liège 1, Belgium*
[4] *Observatoire de Genève, Université de Genève, 51 Chemin des Maillettes, 1290 Sauverny, Switzerland*
[5] *Department of Physics and Astronomy, University of Leicester, Leicester, LE1 7RH, UK*
[6] *Astrophysics Research Centre, School of Mathematics & Physics, Queen's University, University Road, Belfast, BT7 1NN, UK*

17 May 2011

ABSTRACT

We report the discovery of three extrasolar planets that transit their moderately bright ($m_V = 12$–13) host stars. WASP-44b is a 0.89-$M_{\rm Jup}$ planet in a 2.42-day orbit around a G8V star. WASP-45b is a 1.03-$M_{\rm Jup}$ planet which passes in front of the limb of its K2V host star every 3.13 days. Weak Ca H+K emission seen in the spectra of WASP-45 suggests the star is chromospherically active. WASP-46b is a 2.10-$M_{\rm Jup}$ planet in a 1.43-day orbit around a G6V star. Rotational modulation of the light curves of WASP-46 and weak Ca H+K emission in its spectra show the star to be photospherically and chromospherically active.

We imposed circular orbits in our analyses as the radial velocity data are consistent with (near-)circular orbits, as could be expected from both empirical and tidal-theory perspectives for such short-period, Jupiter-mass planets. We discuss the impact of fitting for eccentric orbits for these type of planets when not supported by the data. The derived planetary and stellar radii depend on the fitted eccentricity and further studies use these quantities in attempts to understand planet structure, the interdependence of parameters and the relevant physics for extrasolar planets. As such, we recommend exercising caution in fitting the orbits of short period, Jupiter-mass planets with an eccentric orbital model when there is no evidence of non-circularity.

Key words: planetary systems – planets and satellites: individual: WASP-44b, WASP-45b, WASP-46b – stars: individual: WASP-44, WASP-45, WASP-46

1 INTRODUCTION

The ensemble of well-characterised transiting extrasolar planets is growing at pace, with over one hundred known to date. It is important to determine the system parameters accurately so that the inferrences on which they are based are reliable. For example, to determine the bulk composition of a planet it is necessary to accurately measure its radius (e.g. Fortney, Marley & Barnes 2007). Many short-period, giant planets (e.g. WASP-17b, Anderson et al. 2010b, 2011) are larger than predicted by standard cooling theory of irradiated, gas-giant planets (e.g. Fortney, Marley & Barnes 2007). One potential explanation

is that energy from the tidal circularisation of eccentric orbits was dissipated within the planets' interiors, causing them to bloat (e.g. Bodenheimer, Lin & Mardling 2001). To evaluate the likelihood that a planet was inflated by such tidal heating, it is necessary to have an accurate determination of both its radius and its orbital eccentricity (e.g. Ibgui, Spiegel & Burrows 2011).

A planet's orbital eccentricity can be determined by measuring the radial motion of its host star across an orbit (e.g. Queloz et al. 2010), or by observing an occultation of a planet by its host star (e.g. Anderson et al. 2011), or from a combination of the two. By combining this eccentricity measurement with high-quality transit light curves, we can measure a star's density (Seager & Mallén-Ornelas 2003). The stellar mass can be estimated using stellar evolu-

tion models (e.g. Demarque et al. 2004) or mass-calibration laws (e.g. Torres, Andersen & Giménez 2010), and the stellar radius follows. This, combined with the ratio of the radii derived from the transit depth, gives the planet radius.

In papers announcing new planet discoveries, eccentricity is often quite poorly determined, thus the planet radius can be quite uncertain. Despite this, there are theoretical (Goldreich & Soter 1966) and empirical (Pont et al. 2011) reasons to expect short-period ($\lesssim 4$ d), Jupiter-mass (≈ 0.5–$2\ M_{\rm Jup}$) planets, often referred to as *hot Jupiters*, to be in circular orbits. Thus it is reasonable, in the absence of evidence to the contrary, to assume that a newly discovered hot Jupiter is in a circular orbit. In so doing, the derived stellar and planetary dimensions will be, on the whole, accurate.

In this paper we present three new hot Jupiters, WASP-44b, WASP-45b and WASP-46b, and discuss the effects of fitting an eccentric orbit model to a hot Jupiter system in the absence of evidence for non-circularity.

2   OBSERVATIONS

2.1   Discovery photometry

The WASP (Wide Area Search for Planets) photometric survey (Pollacco et al. 2006) employs two eight-camera arrays, each with a field of view of 450 deg^2, to monitor bright stars ($m_{\rm V} = 8$–15). Each array observes up to eight pointings per night with a cadence of 5–10 min, and each pointing is followed for around five months at a time. The WASP-South station (Hellier et al. 2011) is hosted by SAAO in South Africa and the SuperWASP-North station (Faedi et al. 2011b) is hosted by the Observatorio del Roque de Los Muchachos on La Palma. The WASP data were processed and searched for transit signals as described in Collier Cameron et al. (2006) and the candidate selection process is described in Collier Cameron et al. (2007).

WASP-44 is a $m_{\rm V} = 12.9$, G8V star located in the constellation Cetus. A transit search of the light curve obtained by WASP-South from 2009 July to November found a weak, 2.42-d periodicity. Further observations in 2008 and 2009 with both WASP instruments led to a total of 15 755 photometric measurements (Figure 1). WASP-44 was also observed by a SuperWASP-North camera during 2010 August to November. The resulting light curve comprises 6 000 measurements and became available during the preparation of this paper. As such, it was not used in determination of the system paramters (Section 4), but was used in the search for rotational modulation (Section 5).

WASP-45 is a $m_{\rm V} = 12.0$, K2V star located in the consellation Sculptor that was observed by WASP-South during May to November of 2006 and 2007. A transit search of the resulting light curve, which comprises 11 007 photometric measurements, found a strong 3.13-d periodicity (Figure 2).

WASP-46 is a $m_{\rm V} = 12.9$, G6V star located in the constellation Indus that was observed by two WASP-South cameras during May to October of 2008 and 2009. A transit search of the resulting light curve, which comprises 41 961 photometric measurements, found a strong 1.43-d periodicity (Figure 2). WASP-46 was also observed by two WASP-South cameras during 2010 August to November. The resulting light curve comprises 19 000 measurements and became
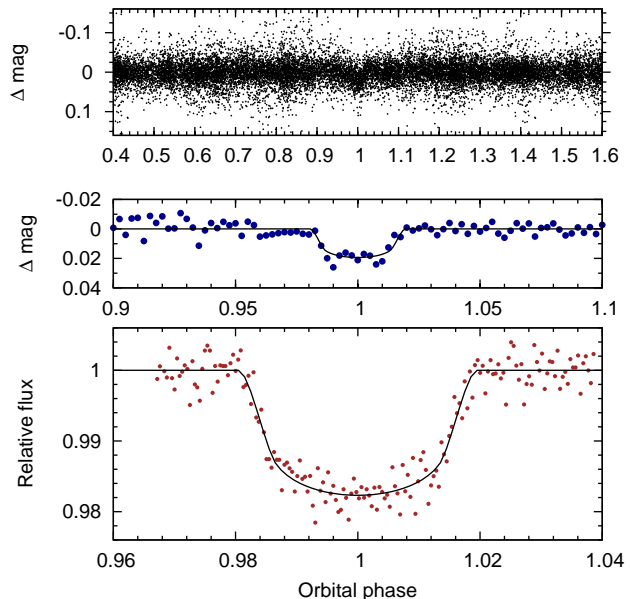

Figure 1. Photometry of WASP-44, with the best-fitting transit model superimposed. **Top:** WASP discovery light curve, folded on the ephemeris of Table 5. **Middle:** WASP data around the transit, binned in time with a bin width of ∼9 min. **Bottom:** High-precision transit light curve from Euler.

available during the preparation of this paper. As such, it was not used in the determination of the system paramters (Section 4), but was used in the search for rotational modulation (Section 5).

WASP-46 is blended in the WASP images with a $m_{\rm V} = 14.8$ star at a separation of $17.4''$ (the plate scale is $13.7''{\rm pixel}^{-1}$ and the photometry aperture has a radius of 3.5 pixels). We corrected the WASP photometry for this contamination to prevent dilution of the transit.

2.2   Spectroscopic follow-up

In 2010 we used the CORALIE spectrograph mounted on the 1.2-m Euler-Swiss telescope (Baranne et al. 1996; Queloz et al. 2000) to obtain spectra of the three target stars. We obtained 17 spectra of WASP-44, 13 spectra of WASP-45 and 16 spectra of WASP-46. Radial-velocity (RV) measurements were computed by weighted cross-correlation (Baranne et al. 1996; Pepe et al. 2005) with a numerical G2-spectral template for both WASP-44 and WASP-46, and with a K5-spectral template for WASP-45. RV variations were detected with the same periods found from the WASP photometry and with semi-amplitudes consistent with planetary-mass companions. The RV measurements are listed in Table 1 and are plotted separately for each system in Figures 4, 5 and 6. We excluded two RVs of WASP-44 from the analysis as the spectra were taken during transit and we do not fit for the Rossiter-McLaughlin effect (e.g. Simpson et al. 2010).

For each system we tested the hypothesis that the RV variations are due to spectral-line distortions caused by a blended eclipsing binary or starspots by performing a line-bisector analysis (Queloz et al. 2001) of the CORALIE
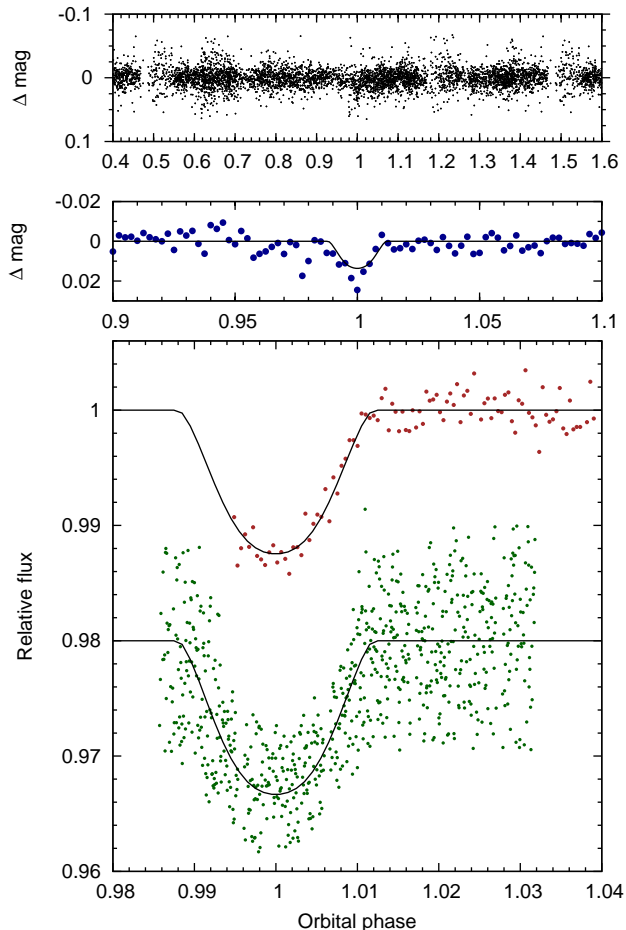
Figure 2. Photometry of WASP-45, with the best-fitting transit model superimposed. **Top:** WASP discovery light curve, folded on the ephemeris of Table 5. **Middle:** WASP data around the transit, binned in time with a bin width of ∼11 min. **Bottom:** High-precision transit light curves from Euler (upper) and TRAPPIST (lower).

Figure 3. Photometry of WASP-46, with the best-fitting transit model superimposed. **Top:** WASP discovery light curve, folded on the ephemeris of Table 5. **Middle:** WASP data around the transit, binned in time with a bin width of ∼5 min. **Bottom:** High-precision transit light curves from TRAPPIST (upper) and Euler (lower).

cross-correlation functions. The lack of correlation between bisector span and RV (Figures 4, 5 and 6) supports our conclusion that the periodic dimming and RV variation of each system are caused by a transiting planet.

2.3 Follow-up photometry

We obtained high signal-to-noise (S/N) transit photometry to refine the parameters of each system. We used the the 1.2-m Euler-Swiss telescope located at ESO La Silla Observatory, Chile to observe one transit each of WASP-44b, WASP-45b and WASP-46b. Observations were made through a Gunn r filter and Euler's absolute tracking mode was used to keep the stars on the same location on the chip. This is done by calculating an astrometric solution for each science frame and adjusting the telescope pointing between exposures. After correcting the images for bias, overscan and flat-field variations, we extracted aperture photometry for the bright stars in the field. We selected the aperture radius and set of reference stars that resulted in the smallest light curve residuals.
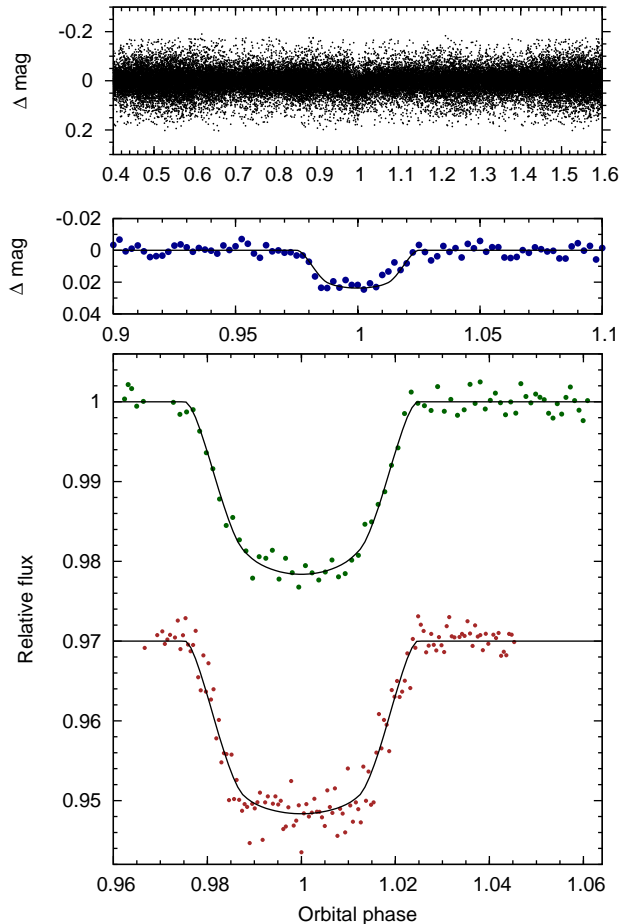
We used TRAPPIST[1], a 60 cm robotic telescope also located at ESO La Silla (Gillon et al. 2011) to observe one transit of WASP-45b and one transit of WASP-46b. Both transits were observed through a special $I+z$ filter, in the 1×2 MHz read-out mode, and with 1×1 binning, resulting in a typical combined readout and overhead time of 8 s and a readout noise of 13.5 e^-. The 'software guiding' system of TRAPPIST kept the stars at the same positions on the chip to within a few pixels over the course of the observations (Gillon et al., in preparation).

2.3.1 WASP-44b

A transit of WASP-44b was observed on 2010 September 14 by Euler. We observed for a total of 4.2 hours, from 46 min before the start of the transit to 65 min after it ended. The conditions were clear, airmass ranged from 1.04 to 1.44 and

Table 1. Radial velocity measurements

Star	BJD (UTC) (day)	RV (km s^{-1})	$\sigma_{\rm RV}$ (km s^{-1})	BS (km s^{-1})
WASP-44	2 455 378.8533	−4.114	0.028	−0.063
WASP-44	2 455 387.7850	−3.923	0.019	−0.011
WASP-44	2 455 388.9089	−4.173	0.024	−0.020
WASP-44	2 455 389.7778	−3.894	0.040	−0.191
WASP-44	2 455 390.7802^a	−4.074	0.025	0.006
WASP-44	2 455 391.8691	−4.095	0.020	−0.156
WASP-44	2 455 392.7604	−3.905	0.023	−0.038
WASP-44	2 455 396.8995	−4.033	0.039	−0.013
WASP-44	2 455 414.8075	−3.981	0.020	−0.026
WASP-44	2 455 446.8271	−4.149	0.027	−0.065
WASP-44	2 455 448.9128^a	−4.013	0.032	−0.005
WASP-44	2 455 449.8568	−4.173	0.024	−0.012
WASP-44	2 455 450.8095	−3.912	0.025	0.001
WASP-44	2 455 451.8089	−4.162	0.025	−0.059
WASP-44	2 455 453.6439	−3.999	0.018	−0.017
WASP-44	2 455 454.8482	−4.049	0.026	−0.069
WASP-44	2 455 482.6600	−3.978	0.025	−0.096
WASP-45	2 455 388.9353	4.406	0.010	−0.044
WASP-45	2 455 390.8149	4.680	0.012	0.030
WASP-45	2 455 391.8937	4.414	0.011	0.016
WASP-45	2 455 392.8314	4.552	0.010	0.012
WASP-45	2 455 393.7593	4.704	0.014	0.013
WASP-45	2 455 404.8466	4.426	0.010	−0.035
WASP-45	2 455 410.7215	4.392	0.019	−0.048
WASP-45	2 455 414.7627	4.557	0.015	−0.011
WASP-45	2 455 446.8614	4.683	0.012	−0.024
WASP-45	2 455 449.8794	4.699	0.011	0.018
WASP-45	2 455 451.8550	4.452	0.015	−0.000
WASP-45	2 455 453.8741	4.507	0.011	−0.004
WASP-45	2 455 482.6826	4.410	0.013	0.033
WASP-46	2 455 334.8428	−3.414	0.029	−0.044
WASP-46	2 455 359.8870	−4.116	0.033	−0.014
WASP-46	2 455 382.7544	−4.092	0.062	0.158
WASP-46	2 455 385.8357	−3.869	0.032	−0.016
WASP-46	2 455 389.8330	−4.144	0.024	−0.075
WASP-46	2 455 390.6889	−3.491	0.036	−0.074
WASP-46	2 455 391.7867	−3.516	0.026	0.057
WASP-46	2 455 392.6562	−4.183	0.031	0.010
WASP-46	2 455 396.7744	−4.058	0.026	−0.033
WASP-46	2 455 400.6822	−3.382	0.027	0.009
WASP-46	2 455 409.6251	−4.025	0.028	0.005
WASP-46	2 455 413.5695	−3.555	0.033	0.082
WASP-46	2 455 414.8452	−3.433	0.047	0.115
WASP-46	2 455 445.6578	−4.141	0.024	−0.092
WASP-46	2 455 449.7606	−4.090	0.036	0.047
WASP-46	2 455 454.7010	−3.513	0.026	−0.083

^{a} These two RVs were excluded from the analysis as they were measured during transit.

no defocus was applied. The WASP-44b transit light curve is shown in Figure 1.

2.3.2   WASP-45b

A partial transit of WASP-45b was observed on 2010 September 11 by Euler. We observed for a total of 3.3 hours, from part-way through the transit to 2 hours after it ended. The seeing was poor (1–2″) and airmass ranged from 1.01 to 1.22. We applied a defocus of 0.1 mm to increase the duty cycle and to minimise pixel-to-pixel effects.

A transit of WASP-45b was observed on 2010 December 17 by TRAPPIST. Observations lasted from 0h15 to 3h40
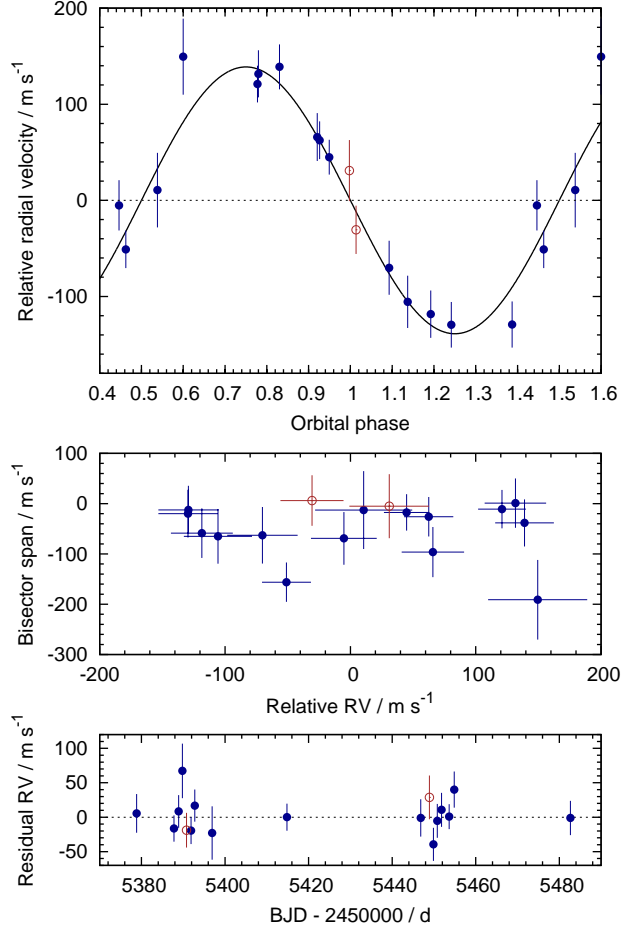

Figure 4. Top: CORALIE RVs of WASP-44 with the best-fitting circular Keplerian orbit superimposed. The RVs represented by open, red circles were excluded from the analysis as they were taken during transit. **Middle:** Bisector span with respect to RV. We adopted uncertainties on the bisector spans twice the size of those on the RVs. **Bottom:** Residuals of the RVs about the fit as a function of time.

UT, during which the airmass increased from 1.03 to 1.73 and the transparency was good. The telescope was strongly defocused to average pixel-to-pixel sensitivity variations and to increase the duty cycle, resulting in a typical full width at half-maximum of the stellar images of ∼9 pixels (∼5.8″). The integration time was 6 s. After a standard pre-reduction (bias, dark and flat-field correction), the stellar fluxes were extracted from the images using the `IRAF/DAOPHOT`[2] aperture photometry software (Stetson 1987). We tested several sets of reduction parameters and chose the set that gave the most precise photometry for the stars of similar brightness to WASP-45. We carefully selected a set of reference stars and then performed differential photometry.

The WASP-45b transit light curves are shown in Figure 2.

Figure 5. Top: CORALIE RVs of WASP-45 with the best-fitting circular Keplerian orbit superimposed. **Middle:** Bisector span with respect to RV. We adopted uncertainties on the bisector spans twice the size of those on the RVs. **Bottom:** Residuals of the RVs about the fit as a function of time.
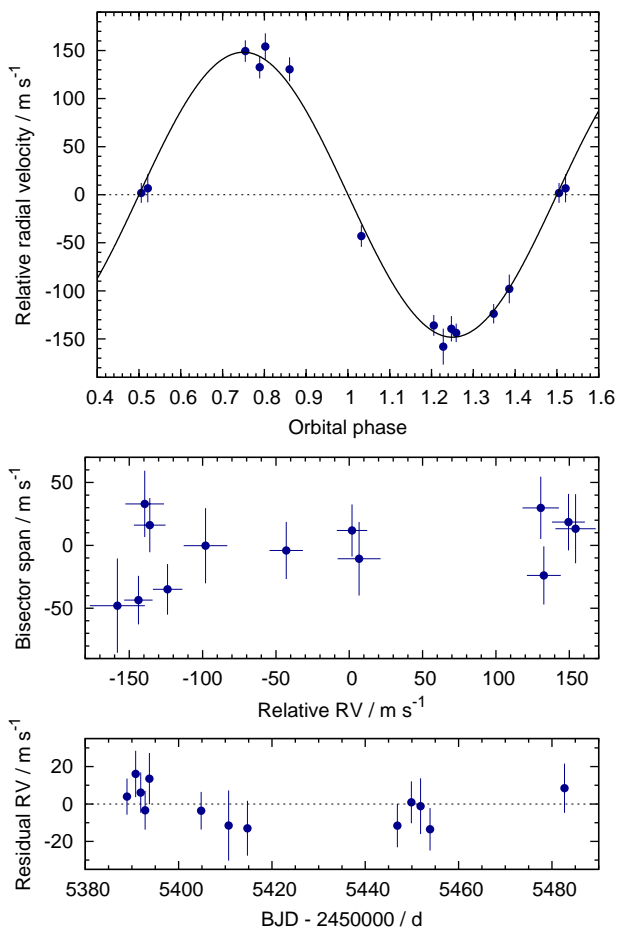

Figure 6. Top: CORALIE RVs of WASP-46 with the best-fitting circular Keplerian orbit superimposed. **Middle:** Bisector span with respect to RV. We adopted uncertainties on the bisector spans twice the size of those on the RVs. **Bottom:** Residuals of the RVs about the fit as a function of time.

2.3.3 WASP-46b

A transit of WASP-46b was observed on 2010 July 19 by TRAPPIST. Observations lasted from 1h15 to 4h05 UT, during which the airmass decreased from 1.83 to 1.22 and the transparency was good. Considering the relative faintness of the target, we chose to keep the telescope focused during the run, and we used an integration time of 60 s. The pre-reduction and reduction procedures were similar to those used for the WASP-45 data.

A transit of WASP-46b was observed on 2010 September 10 by Euler. We observed for a total of 3.4 hours, from 35 min before the start of transit to 75 min after it ended. The conditions were variable and airmass increased from 1.12 to 1.4 during the observations. No defocus was applied.

The WASP-46b transit light curves are shown in Figure 3.

3 STELLAR PARAMETERS FROM SPECTRA

For each system, the CORALIE spectra were co-added to produce a single spectrum with a typical S/N of around 50:1. The analysis was performed using the methods given
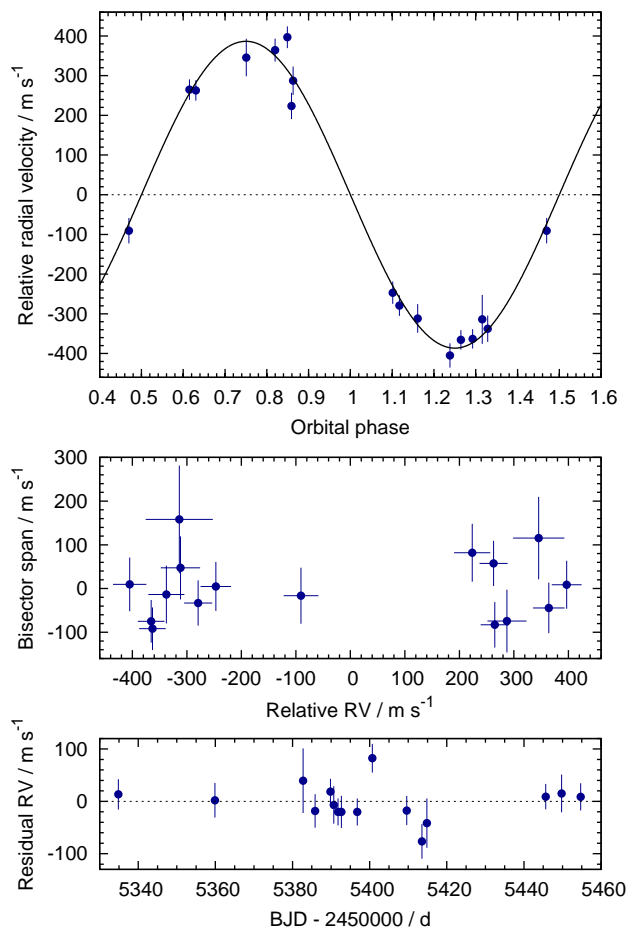
in Gillon et al. (2009). The $H\alpha$ line was used to determine the effective temperature ($T_{\rm eff}$), while the Na I D and Mg I b lines were used as surface gravity ($\log g_*$) diagnostics. The parameters obtained from the analysis are given in Table 2. The elemental abundances were determined from equivalent-width measurements of several clean and unblended lines. A value for microturbulence ($\xi_{\rm t}$) was determined from Fe I using the method of Magain (1984). The quoted error estimates include that given by the uncertainties in $T_{\rm eff}$, $\log g_*$ and $\xi_{\rm t}$, as well as the scatter due to measurement and atomic data uncertainties.

The projected stellar rotation velocities ($v \sin I$) were determined by fitting the profiles of several unblended Fe I lines. For this we used an instrumental FWHM of 0.11 ± 0.01 Å, determined from the telluric lines around 6300Å, and used the Bruntt et al. (2010) calibration to assume values for macroturbulence ($v_{\rm mac}$). The $v_{\rm mac}$ values we assumed were 1.4 ± 0.3 km s^{-1} for WASP-44, 0.7 ± 0.3 km s^{-1} for WASP-45, and 2.0 ± 0.3 km s^{-1} for WASP-46.

Though the S/N are very low in the Ca H+K regions of our spectra, we searched for signs of emission, which would be indicative of stellar chromospheric activity. The WASP-

Table 2. Stellar parameters from spectra

Parameter (Unit)	WASP-44	WASP-45	WASP-46
$T_{\rm eff}$ (K)	5400 ± 150	5100 ± 200	5600 ± 150
$\log g_*$ (cgs)	4.5 ± 0.2	4.4 ± 0.2	4.4 ± 0.2
$\xi_{\rm t}$ (km s^{-1})	1.0 ± 0.2	0.5 ± 0.3	1.0 ± 0.2
$v \sin I$ (km s^{-1})	3.2 ± 0.9	2.3 ± 0.7	1.9 ± 1.2
[Fe/H]	0.06 ± 0.10	0.36 ± 0.12	-0.37 ± 0.13
[Na/H]	0.24 ± 0.09	0.56 ± 0.14	-0.35 ± 0.09
[Mg/H]	0.25 ± 0.07	0.57 ± 0.09	-0.10 ± 0.10
[Al/H]	0.20 ± 0.13	0.45 ± 0.11	-0.24 ± 0.08
[Si/H]	0.25 ± 0.13	0.50 ± 0.15	-0.27 ± 0.10
[Ca/H]	0.10 ± 0.17	0.38 ± 0.17	-0.21 ± 0.13
[Sc/H]	0.30 ± 0.17	0.45 ± 0.27	-0.13 ± 0.16
[Ti/H]	0.12 ± 0.10	0.46 ± 0.20	-0.29 ± 0.18
[V/H]	0.24 ± 0.17	0.73 ± 0.18	-0.21 ± 0.21
[Cr/H]	0.13 ± 0.07	0.34 ± 0.12	-0.31 ± 0.12
[Mn/H]	0.29 ± 0.10	0.93 ± 0.24	-0.47 ± 0.14
[Co/H]	0.23 ± 0.09	0.70 ± 0.11	-0.32 ± 0.24
[Ni/H]	0.13 ± 0.12	0.51 ± 0.16	-0.39 ± 0.10
$A_{\rm Li}$	< 1.0	< 0.8	< 0.8
M_* ($M_\odot$)	0.95 ± 0.08	0.95 ± 0.10	0.93 ± 0.09
R_* ($R_\odot$)	0.90 ± 0.22	1.00 ± 0.25	1.00 ± 0.26
Spec. Type	G8V	K2V	G6V
Gyro. Age	$0.9^{+1.0}_{-0.6}$	$1.4^{+2.0}_{-1.0}$	$1.4^{+0.4}_{-0.6}$
R.A. (J2000)	$00^{\rm h}15^{\rm m}36\overset{\rm s}{.}76$	$00^{\rm h}20^{\rm m}56\overset{\rm s}{.}99$	$21^{\rm h}14^{\rm m}56\overset{\rm s}{.}86$
Dec. (J2000)	$-11°56'17\overset{''}{.}4$	$-35°59'53\overset{''}{.}8$	$-55°52'18\overset{''}{.}1$
$m_{\rm V}$	12.9	12.0 ± 0.2	12.9
$m_{\rm J}$[a]	11.70 ± 0.02	10.75 ± 0.02	11.75 ± 0.02
$m_{\rm H}$[a]	11.41 ± 0.03	10.37 ± 0.03	11.47 ± 0.03
$m_{\rm K}$[a]	11.34 ± 0.03	10.29 ± 0.02	11.40 ± 0.03
2MASS[a]	$00153675-1156172$	$00205699-3559537$	$21145687-5552184$

[a] Skrutskie et al. (2006).

44 spectra show no signs of emission and both the WASP-45 and WASP-46 spectra show weak emission.

We input our values of $T_{\rm eff}$, $\log g_*$ and [Fe/H] into the calibrations of Torres, Andersen & Giménez (2010) to obtain estimates of the stellar mass and radius.

We used the method of Barnes (2007) to estimate gyrochronological ages for the stars. For WASP-44 and WASP-45 we calculated rotation periods from our $v \sin I$ determinations. If either star is inclined with respect to the sky plane then it will be rotating faster than suggested by $v \sin I$ and so is likely to be younger than indicated. For WASP-46, the rotation period found from the modulation of the WASP light curves was used (see Section 5). As such, the age estimate for this star is not a limit.

4 SYSTEM PARAMETERS FROM RV AND TRANSIT DATA

4.1 WASP-44b and WASP-46b

We determined the parameters of each system from a simultaneous fit to all data. The fit was performed using the current version of the Markov-chain Monte Carlo (MCMC) code described by Collier Cameron et al. (2007) and Pollacco et al. (2008).

The transit light curves were modelled using the formulation of Mandel & Agol (2002) with the assumption that the planet is much smaller than the star. Limb-darkening was accounted for using a four-coefficient, nonlinear limb-darkening model, using coefficients appropriate to the passbands from the tabulations of Claret (2000, 2004). The coefficients were interpolated once using the values of $\log g_*$ and [Fe/H] in Table 2, but were interpolated at each MCMC step using the latest value of $T_{\rm eff}$. The coefficient values corresponding to the best-fitting value of $T_{\rm eff}$ are given in Table 3. The transit light curve is parameterised by the epoch of mid-transit T_0, the orbital period P, the planet-to-star area ratio $(R_{\rm pl}/R_*)^2$, the approximate duration of the transit from initial to final contact T_{14}, and the impact parameter $b = a \cos i/R_*$ (the distance, in fractional stellar radii, of the transit chord from the star's centre in the case of a circular orbit), where a is the semimajor axis and i is the inclination of the orbital plane with respect to the sky plane.

The eccentric Keplerian radial-velocity orbit is parameterised by the stellar reflex velocity semi-amplitude K_1, the systemic velocity γ, and $\sqrt{e} \cos \omega$ and $\sqrt{e} \sin \omega$ (Collier Cameron, in preparation), where e is orbital eccentricity and ω is the argument of periastron.

The linear scale of the system depends on the orbital separation a which, through Kepler's third law, depends on the stellar mass M_*. At each step in the Markov chain, the latest values of ρ_*, $T_{\rm eff}$ and [Fe/H] are input in to the empirical mass calibration of Enoch et al. (2010) to obtain M_*. The shapes of the transit light curves and the radial-velocity curve constrain ρ_* (Seager & Mallén-Ornelas 2003), which combines with M_* to give R_*. $T_{\rm eff}$ and [Fe/H] are proposal

Table 3. Limb-darkening coefficients

Planet	Instrument	Observation bands	Claret band	a_1	a_2	a_3	a_4
WASP-44	WASP / Euler	Broad (400–700 nm) / Gunn r	Cousins R	0.646	-0.437	1.080	-0.519
WASP-45	WASP / Euler	Broad (400–700 nm) / Gunn r	Cousins R	0.755	-0.768	1.450	-0.623
WASP-45	TRAPPIST	Cousins I+Sloan z'	Sloan z'	0.833	-0.891	1.304	-0.547
WASP-46	WASP / Euler	Broad (400–700 nm) / Gunn r	Cousins R	0.543	-0.055	0.592	-0.348
WASP-46	TRAPPIST	Cousins I+Sloan z'	Sloan z'	0.630	-0.371	0.727	-0.366

parameters constrained by Gaussian priors with mean values and variances derived directly from the stellar spectra (see Section 3).

As the planet-star area ratio is determined from the measured transit depth, $R_{\rm pl}$ follows from R_*. The planet mass $M_{\rm pl}$ is calculated from the the measured value of K_1 and the value of M_*; the planetary density $\rho_{\rm pl}$ and surface gravity $\log g_{\rm pl}$ then follow. We also calculate the planetary equilibrium temperature $T_{\rm eql}$, assuming zero albedo and efficient redistribution of heat from the planet's presumed permanent day side to its night side, and the ingress and egress durations, T_{12} and T_{34}.

At each step in the MCMC procedure, model transit light curves and radial velocity curves are computed from the proposal parameter values, which are perturbed from the previous values by a small, random amount. The χ^2 statistic is used to judge the goodness of fit of these models to the data and a step is accepted if χ^2 is lower than for the previous step. A step with higher χ^2 is accepted with a probability proportional to $\exp(-\Delta\chi^2/2)$, which gives the procedure some robustness against local minima and leads to the thorough exploration of the parameter space around the best-fitting solution. To give proper weighting to each photometry data set, the uncertainties were scaled at the start of the MCMC so as to obtain a photometric reduced-χ^2 of unity. For the same reason, a jitter term of $10.2 \ {\rm m\,s}^{-1}$ was added in quadrature to the formal errors of the WASP-46 RVs. A possible source of this jitter is stellar activity, as indicated by chromospheric and photometric indicators (Sections 3 and 5). With reduced spectroscopic χ^2 values of less than unity, it was not necessary to add any jitter to the RVs of WASP-44.

4.2 WASP-45b

The analysis for WASP-45b was the same as for WASP-44b and WASP-46b, except we used evolutionary models to impose priors on stellar mass and density for reasons to be explained.

The apparent lack of second and third contact points in the transit light curves of WASP-45b (Figure 2) indicate that the transit is grazing or near-grazing. When b + $R_{\rm pl}/R_*$ > 1, the planet does not fully pass in front of the star. Thus, as b tends toward higher values, $R_{\rm pl}$ must inflate so that the ratio $R_{\rm pl}/R_*$ remains consistent with the observed transit depth. Also, R_* must inflate so as to remain consistent with the observed transit duration. This results in stellar and planetary radii that are non-physical in a sizeable portion of accepted MCMC steps.

To avoid biasing the derived stellar and planetary radii to larger values, we imposed a prior on stellar density us-
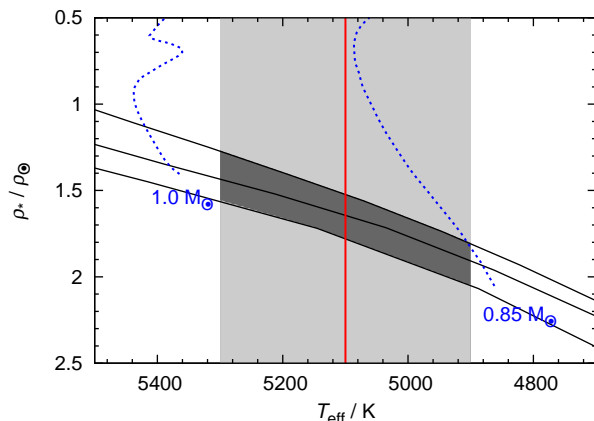

Figure 7. Evolutionary diagram for WASP-45 with the models of Demarque et al. (2004). The solid, black lines are isochrones, with the ages coming from gyrochronology: [Fe/H] = 0.48, 3.4 Gyr (top); [Fe/H] = 0.36, 1.4 Gyr (middle); [Fe/H] = 0.24, 0.4 Gyr (bottom). The two dashed, blue lines are the mass tracks for 1.0 $M_\odot$ with [Fe/H] = 0.48 and 0.85 $M_\odot$ with [Fe/H] = 0.24. The isochrones and mass tracks we chose to display are those that bound the region of interest, which is the area shaded dark grey that indicates the range of stellar densities consistent with the models. The solid, red line indicates our best-fitting $T_{\rm eff}$, and the area shaded light grey corresponds to the 1-σ confidence interval.

ing the constraints provided by our gyrochronological age determination (Table 2) and evolutionary models. Our gyrochronolgical age is determined using $v \sin I$ and so is an upper limit. If the stellar spin axis is inclined with respect to the sky plane then the star will truly be rotating faster and will therefore be younger. We plotted the isochrones and mass tracks of Demarque et al. (2004) relevant to the value ranges we obtained for $T_{\rm eff}$, [Fe/H] and age (Figure 7). By interpolating the models for these measured values, we obtained stellar dimensions consistent with the models: $\rho_* = 1.65 \pm 0.40 \ \rho_\odot$ and $M_* = 0.91 \pm 0.06 \ M_\odot$. We used these values to place Gaussian priors, by means of Bayesian penalties on χ^2, at each MCMC step.

It was not necessary to add any jitter to the RVs of WASP-45.

4.3 The imposition of circular orbits

For each system, the best-fitting eccentricity is small and consistent with zero (Table 4). We used the F-test approach of Lucy & Sweeney (1971) to calculate the probability, $\mathbb{P}_{\rm LS}$, that the improvement in the fit that results from fitting for an eccentric orbit could have arisen by chance if the under-

lying orbit were circular. For each system, we found $\mathbb{P}_{LS}$ to be much higher (Table 4) than the threshold of 0.05 suggested by Lucy & Sweeney (1971), below which they consider the detection of a non-zero eccentricity to be significant. In the absence of conclusive evidence to the contrary, we assumed the orbit of each planet to be circular in producing the adopted solutions that we present. This issue is dealt with at greater length in the discussion.

4.4   Results

The median values and 1-σ uncertainties of the system parameters derived from the MCMC model fits are presented in Table 5. The corresponding transit models are superimposed on the transit photometry in Figures 1, 2 and 3. The corresponding orbit models are superimposed on the radial velocities in Figures 4, 5 and 6, in which we also show the RV residuals as a function of time. From the residual plots one can evaluate both the level to which stellar activity may have affected the RVs and the evidence for a third body. The RVs of each planet-hosting star, obtained over the course of 100 days, show no evidence for motion induced by a third body. The residuals of WASP-46 show greater scatter ($\chi^2 = 19.2$ for WASP-46 compared to 10.9 for WASP-44 and 7.4 for WASP-45), which is probably due to the star being active (see Sections 3 and 5).

We also performed MCMCs fitting an eccentric model to the RVs so as to illustrate the impact on those parameters that are liable to be affected when imposing a circular orbit. The best-fitting values and associated uncertainties from MCMCs fitting an eccentric model are given in Table 4, and these are to be compared with the values of our adopted solutions in Table 5, derived using a circular model. As the eccentricity is quite well constrained by the RV data and as the best-fitting eccentricity values are small, the best-fitting parameter values and their uncertainties are affected little by the imposition of a circular orbit.

5   ROTATIONAL MODULATION

We analysed the WASP light curves of each star to determine whether they show periodic modulation due to the combination of magnetic activity and stellar rotation. We used the sine-wave fitting method described in Maxted et al. (2010) to calculate periodograms such as those shown in the upper panels of Figure 8. These are calculated over 4 096 uniformly spaced frequencies from 0 to 1.5 cycles day^{-1}. The false alarm probability levels shown in these figures are calculated using a boot-strap Monte Carlo method also described in Maxted et al. (2010). Variability due to star spots is not expected to be coherent on long timescales as a consequence of the finite lifetime of star-spots and differential rotation in the photosphere so we analysed each season of data separately.

We found no evidence of rotational modulation in any of the WASP-44 or WASP-45 light curves.

We applied the sine-wave fitting method to the WASP-46 light curves from each of the three seasons to produce the periodograms in the upper panels of Figure 8. The peaks in the periodograms for the first two seasons of data are highly significant and imply periods of 16.55 ± 0.10 d and

14.92 ± 0.07 d. We used a boot-strap Monte Carlo method to estimate the errors on these periods. The periodogram for the third season of data shows peaks corresponding to a period of 8.08 d. Our boot-strap Monte Carlo method fails to provide a reliable estimate for this less significant peak. The amplitudes of the variations estimated from the sine-wave fits are in the range of 3–5 milli-magnitudes (Fig. 8, lower panels). We also calculated periodograms of two stars with similar magnitudes and colours to WASP-46 observed simultaneously with the same camera. Neither of these stars showed significant periodic modulation in the same frequency interval with the exception of one season of data for one star that showed significant power close to 1 cycle day^{-1}, the source of which is likely to be diurnal.

Our interpretation of these results is that the WASP light curve of WASP-46 does show periodic modulation due to the rotation of the star with a period of 16 ± 1 days. The period of 8.08 days derived from the third season of data can be explained by the distribution of star spots during this season resulting in a light curve with two minima per cycle. Similarly, the poorly defined peak in the periodogram for the second season of data may be due to the appearance and disappearance of star spot groups during the observing season.

Using the rotational-modulation period of 16 ± 1 days and the stellar radius from Table 5, we calculate the stellar rotation velocity v to be 2.9 ± 0.2 km s^{-1}. That this value is higher than the value of $v \sin I$ (1.9 ± 1.2 km s^{-1}) determined from spectral line profiles (Table 2) suggests that the stellar spin axis is inclined by $I = 41 \pm 40°$ with respect to the sky plane. This should be appreciated when assessing whether a measurement of WASP-46b's Rossiter-McLaughlin effect is indicative of an aligned or a misaligned orbit (e.g. Schlaufman 2010). Usually only the sky-projected angle between the planetary orbit and stellar spin axis can be determined, but with a measurement of I the true angle can be determined. Our measurement of I would be improved by a more precise determination of spectroscopic $v \sin I$.

6   DISCUSSION

WASP-44b is a 0.89-M_{Jup} planet in a 2.42-day orbit around a solar metallicity ([Fe/H] $= 0.06 \pm 0.10$) G8V star. The star is observable from both hemispheres and seems to be inactive as it shows no signs of rotational modulation or Ca H+K emission.

WASP-45b is a Jupiter-mass planet that partially transits its metal rich ([Fe/H] $= 0.36 \pm 0.12$) K2V host star every 3.13 days. The (near-)grazing nature of the transits led us to impose a prior on the density of the host star so that the derived stellar and planetary radii are physical. The star may be active as weak Ca H+K emission is seen in its spectra, though no rotational modulation is evident in the light curves.

WASP-46b is a 2.10-M_{Jup} planet in a 1.43-day orbit around a metal poor ([Fe/H] $= -0.37 \pm 0.13$) G6V star. We found the star to be active as weak Ca H+K emission is present in its spectra and a clear 16-day rotational modulation signature is evident in the WASP light curves. The slower rotation rate suggested by spectrocopic $v \sin I$ indi-

Table 4. The limits placed on orbital eccentricity and the impact of fitting for it

Parameter (Unit)	WASP-44	WASP-45	WASP-46
e	$0.036^{+0.054}_{-0.025}$	$0.023^{+0.027}_{-0.016}$	$0.018^{+0.021}_{-0.013}$
$\mathbb{P}_{\mathrm{LS}}$	0.51	1	0.67
e (2 σ upper limit)	< 0.172	< 0.095	< 0.065
e (3 σ upper limit)	< 0.263	< 0.148	< 0.092
ω (°)	-59^{+132}_{-47}	21^{+59}_{-94}	$65._{-122}^{+50}$
$e\cos\omega$	$0.003^{+0.023}_{-0.018}$	$0.010^{+0.015}_{-0.011}$	$0.001^{+0.014}_{-0.010}$
$e\sin\omega$	$-0.011^{+0.028}_{-0.069}$	$0.003^{+0.034}_{-0.019}$	$0.008^{+0.026}_{-0.012}$
$\phi_{\mathrm{mid-occultation}}$	$0.502^{+0.015}_{-0.012}$	$0.5061^{+0.0096}_{-0.0067}$	$0.5007^{+0.0087}_{-0.0066}$
T_{58} (d)	$0.0915^{+0.0049}_{-0.0093}$	$0.0711^{+0.0055}_{-0.0073}$	$0.07008^{+0.00089}_{-0.00104}$
$T_{56} \approx T_{78}$ (d)	$0.0132^{+0.0033}_{-0.0030}$	> 0.0257	$0.0184^{+0.0029}_{-0.0018}$
M_* ($M_\odot$)	0.948 ± 0.034	0.910 ± 0.060	0.957 ± 0.034
R_* ($R_\odot$)	$0.892^{+0.085}_{-0.097}$	$0.950^{+0.093}_{-0.074}$	0.928 ± 0.034
ρ_* ($\rho_\odot$)	$1.33^{+0.54}_{-0.30}$	1.06 ± 0.27	1.20 ± 0.12
M_{pl} (M_{Jup})	$0.893^{+0.071}_{-0.066}$	1.005 ± 0.053	2.100 ± 0.073
R_{pl} (R_{Jup})	$1.09^{+0.13}_{-0.14}$	$1.17^{+0.28}_{-0.14}$	1.327 ± 0.058
ρ_{pl} (ρ_{Jup})	$0.69^{+0.37}_{-0.20}$	0.64 ± 0.30	0.90 ± 0.12

This table demonstrates the effects of fitting for orbital eccentricity and is to be compared with Table 5, which presents our adopted solutions.

Table 5. System parameters from RV and transit data from our adopted, circular solutions

Parameter (Unit)	WASP-44	WASP-45	WASP-46
P (d)	2.4238039 ± 0.0000087	3.1260876 ± 0.0000035	1.4303700 ± 0.0000023
T_0 (HJD, UTC)	$2\,455\,434.376 \pm 0.00040$	$2\,455\,441.26925 \pm 0.00058$	$2\,455\,392.31553 \pm 0.00020$
T_{14} (d)	0.0936 ± 0.0022	0.0746 ± 0.0035	0.06973 ± 0.00090
$T_{12} = T_{34}$ (d)	0.0146 ± 0.0026	> 0.0270	0.0178 ± 0.0013
a/R_*	$8.05^{+0.66}_{-0.52}$	9.22 ± 0.74	5.74 ± 0.15
R_{pl}^2/R_*^2	0.01588 ± 0.00076	0.01495 ± 0.00071	0.02155 ± 0.00049
b	$0.560^{+0.076}_{-0.123}$	$0.888^{+0.045}_{-0.026}$	0.737 ± 0.019
i (°)	$86.02^{+1.11}_{-0.86}$	$84.47^{+0.54}_{-0.79}$	82.63 ± 0.38
K_1 (m s^{-1})	138.8 ± 9.0	148.3 ± 4.1	387 ± 10
γ (m s^{-1})	$-4\,043.82 \pm 0.71$	$4\,549.95 \pm 0.63$	$-3\,778.3 \pm 1.1$
e	0 (adopted)	0 (adopted)	0 (adopted)
M_* ($M_\odot$)	0.951 ± 0.034	0.909 ± 0.060	0.956 ± 0.034
R_* ($R_\odot$)	$0.927^{+0.068}_{-0.074}$	$0.945^{+0.087}_{-0.071}$	0.917 ± 0.028
$\log g_*$ (cgs)	$4.481^{+0.068}_{-0.057}$	$4.445^{+0.065}_{-0.075}$	4.493 ± 0.023
ρ_* ($\rho_\odot$)	$1.19^{+0.32}_{-0.22}$	$1.08^{+0.27}_{-0.24}$	1.24 ± 0.10
T_{eff} (K)	5410 ± 150	5140 ± 200	5620 ± 160
[Fe/H]	0.06 ± 0.10	—	-0.37 ± 0.13
M_{pl} (M_{Jup})	0.889 ± 0.062	1.007 ± 0.053	2.101 ± 0.073
R_{pl} (R_{Jup})	1.14 ± 0.11	$1.16^{+0.28}_{-0.14}$	1.310 ± 0.051
$\log g_{\mathrm{pl}}$ (cgs)	$3.197^{+0.094}_{-0.082}$	$3.23^{+0.11}_{-0.19}$	3.447 ± 0.033
ρ_{pl} (ρ_{Jup})	$0.61^{+0.23}_{-0.15}$	0.64 ± 0.30	0.94 ± 0.11
a (AU)	0.03473 ± 0.00041	0.04054 ± 0.00090	0.02448 ± 0.00028
$T_{\mathrm{pl,A=0}}$ (K)	1343 ± 64	1198 ± 69	1654 ± 50

cates that the stellar spin axis is inclined relative to the sky plane ($I = 41 \pm 40°$). By observing WASP-46b's Rossiter-McLaughlin effect (e.g. Simpson et al. 2010), which is predicted to have an amplitude of 18 m s^{-1}, we could thus measure the true angle between the stellar spin and the plane-

tary orbit axes, rather than just the sky-projected angle. The large size of the planet, the high stellar insolation, and the relative lateness of the host star make WASP-46b a good target for infrared occultation photometry (e.g. Anderson et al. 2011) .
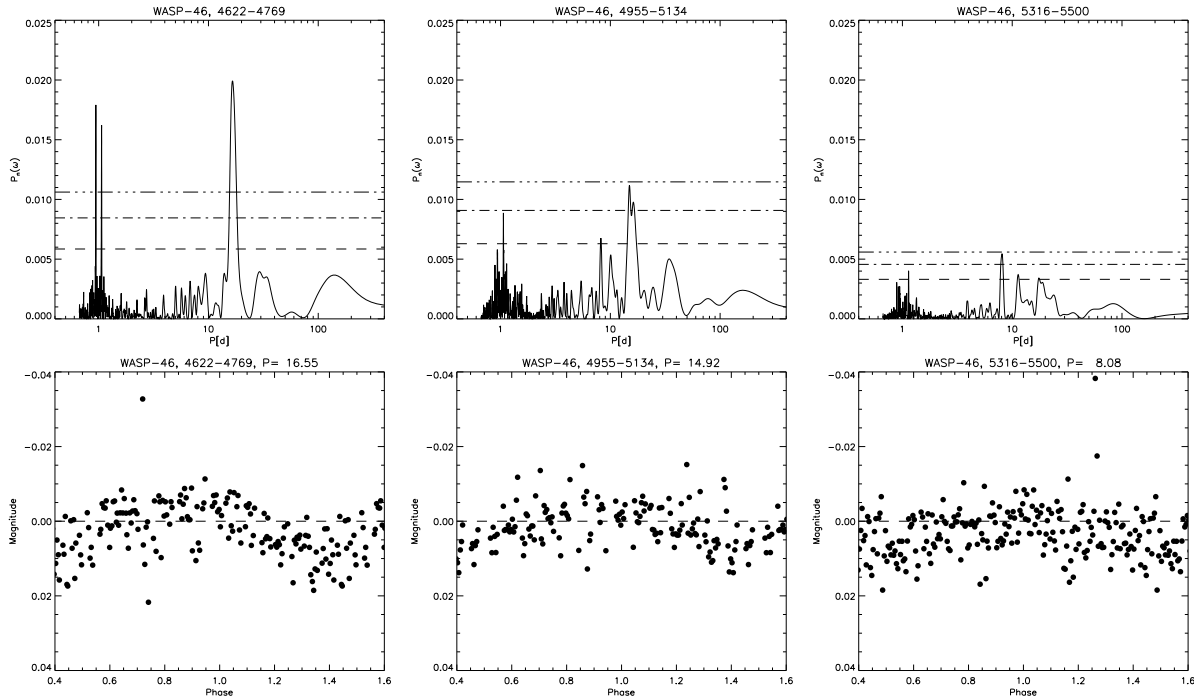
Figure 8. *Upper panels*: Periodograms for the WASP data from three seasons for WASP46. The date range (JD−245000) is given in the title of each panel. Horizontal lines indicate false alarm probability levels FAP=0.1, 0.01, 0.001. *Lower panels*: Data folded and binned in 0.005 phase bins for the periods noted alongside the date range in the plot title.

The upper limits placed on the lithium abundances suggest that each star is at least a few Gyr old (Table 2; Sestito & Randich 2005), which is in contrast with the gyrochronological ages of ∼0.9–1.4 Gyr.

6.1   Fit for eccentricity or impose a circular orbit?

To date, over one hundred transiting planets are known and many more will be discovered in the coming years. The determination of a planet's bulk composition requires the accurate and precise measurement of its radius, which is only possible for transiting planets. To accurately determine the radius of a transiting planet it is necessary to acquire high-quality transit light curves and to measure orbital eccentricity. For those planets with poorly constrained eccentricity, further radial-velocity and occultation-timing measurements are necessary. However, these will be performed slowly and perhaps only for a fraction of systems.

Around half of all known transiting planets are hot Jupiters ($P \lesssim 4$ d and $M_{\rm pl} \approx 0.5$–$2\ M_{\rm Jup}$), and Pont et al. (2011) find no evidence for an eccentric orbit among these. Further, tidal theory predicts that the timescale of tidal circularisation is a sharp function of semimajor axis and planet radius, and a weaker function of planetary and stellar masses (Goldreich & Soter 1966). That is, low-mass, bloated planets in short orbits around high-mass stars are expected to circularise quickest. So, there is a theoretical basis and an empirical basis for expecting a newly-discovered hot Jupiter to be in a circular orbit.

When a hot Jupiter is first announced the radial velocity data often poorly constrain eccentricity, and occultation observations are almost never available. In those circum-

stances, some authors have opted to impose a circular orbit (e.g.: Anderson et al. 2010a; Faedi et al. 2011a), as is theoretically and empirically reasonable, though doing so does artificially reduce the uncertainties on the system paramters. If, as seems to be the case, the majority of hot Jupiters are in near-circular orbits, then this is, *a posteriori*, a reasonable course of action. Though further measurements will show some planets to have a small, non-zero eccentricity, for the majority eccentricity will be constrained to ever-smaller values consistent with zero. Other authors have opted to fit for an eccentric orbit (e.g.: Hellier et al. 2010; Bakos et al. 2010) so as to obtain more conservative error bars. Fitting an eccentric orbit model to RV measurements of a (near-)circular orbit will always result in a non-zero value of e (e.g. Laughlin et al. 2005), and this can affect the derived stellar and planetary parameters. As compared to the circular solution, the eccentric solution will typically change the planet's speed during transit and, as the transit duration is fixed by measurement, a change in speed necessitates a change in distance travelled during transit, i.e. the derived stellar radius. In turn, as the ratio of planetary-to-stellar radii is fixed by the measured transit depth, then the derived planet radius is changed.

Being aware of these issues, some authors have opted to present both a circular solution, which is most likely, and an eccentric solution, which gives an honest account of the uncertainties in the data (e.g. Anderson et al. 2010b). One issue with this approach is that many authors tend to prefer to work with a single solution and so will adopt the one they favour regardless. Another approach is to present the best-fitting parameter values from a circular fit and the error bars from an eccentric fit (e.g.: Enoch et al. 2011; Maxted et al.

2010). Thus the most likely solution is presented with conservative error bars, but care should be taken to calculate the 1-σ confidence intervals in the posterior probability distributions about the best-fitting circular values.

Unless there is clear evidence for an eccentric orbit, we recommend imposing a circular orbit when deriving the parameters of a system containing a hot Jupiter. This will avoid creep in the literature of parameter values as further RV and occultation observations show discovery-paper eccentricities to be spurious. There may well be occasions when evidence for an eccentric orbit is found for a planet for which there previously was none, but this will be a more minor, interesting correction. When the uncertainties from the eccentric solution are significantly bigger, authors might choose to present those together with the best-fitting parameter values from the circular solution. Alternatively, the values of potentially-affected parameters could be presented from both the circular and the eccentric solutions, as was done in this paper. When eccentricity is reasonably well-constrained to small values, then the difference in the best-fitting parameters and the size of the uncertainties will be small. It will then matter little which solution is presented, as is the case for the three planets presented herein. Presenting an upper limit (e.g. 3 σ) on eccentricity shows how well constrained the parameter is and, for example, permits the upper limit of the tidal heating rate to be calculated.

As the best-fitting eccentricity values for the three systems presented in this paper are small ($e = 0.02$–0.04) the differences between the best-fitting parameter values from circular and from eccentric solutions are small (compare Tables 4 and 5). However, eccentricity is often poorly determined in a discovery paper and the choice to fit for eccentricity then has a greater impact. An illustrative example is the case of WASP-17b. In the discovery paper (Anderson et al. 2010b), we presented three solutions, including one with an imposed circular orbit which gave $R_{\rm pl} = 1.97 \pm 0.10\ R_{\rm Jup}$, and another, which we adopted as our preferred solution, in which we fit for an eccentric orbit that gave $R_{\rm pl} = 1.74^{+0.26}_{-0.23}$ $R_{\rm Jup}$ and $e = 0.129^{+0.106}_{-0.068}$. We had initially favoured the circular solution as theory suggested this as the most likely and the additional two free parameters of an eccentric orbit did not significantly improve the fit. However, we adopted the eccentric solution due to its more conservative error bars. We had been able to place only a weak constraint on eccentricity as the low mass of the planet (0.49 $M_{\rm Jup}$) and the high effective surface temperature of the star (6650 K) caused our measurement of the reflex motion of the star to be quite low S/N. This situation improved when we observed two occultations of WASP-17b, which we used to show the orbit of WASP-17b to be very slightly eccentric ($e \approx 0.0055$ Anderson et al. 2011) and the planet radius to be $1.991 \pm 0.081\ R_{\rm Jup}$. As such, the circular solution that we presented in the discovery paper was closest to describing the system and we would have done better to have adopted that.

By the time we had shown the orbit of WASP-17b to be near-circular, a number of papers had, at least in part, based their models, results or conclusions on the values of one or both of e and R_* of the discovery paper's adopted solution (e.g.: Schlaufman 2010; Hansen 2010; Cowan & Agol 2011; Ehrenreich & Désert 2011). Though it is true that our updated solution was not excluded, not even at the 1-σ level,

some of those studies had only considered WASP-17 due to its apparent significant eccentricity, and other such works were sure to follow. For example, the possibility that tidal dissipation could have inflated WASP-17b would probably have been tested as was done by Ibgui, Spiegel & Burrows (2011) for other systems. Before we showed the planet to be even more bloated than first suggested and placed a much tighter constraint on eccentricity, tidal heating had seemed a much more likely explanation for the anomalously large size of WASP-17b.

The accurate determination of orbital eccentricities and planetary and stellar radii is key to the understanding of planet structure, the interdependence of parameters and the relevant physics for extrasolar planets. As such, we should make every effort to avoid introducing biases into the sample that we have to work with.

REFERENCES

Anderson D. R. et al., 2010a, arXiv:1011.5882
—, 2010b, ApJ, 709, 159
—, 2011, arXiv:1101.5620
Bakos G. Á. et al., 2010, arXiv:1008.3388
Baranne A. et al., 1996, A&AS, 119, 373
Barnes S. A., 2007, ApJ, 669, 1167
Bodenheimer P., Lin D. N. C., Mardling R. A., 2001, ApJ, 548, 466
Bruntt H. et al., 2010, MNRAS, 405, 1907
Carlsson M., Rutten R. J., Bruls J. H. M. J., Shchukina N. G., 1994, A&A, 288, 860
Claret A., 2000, A&A, 363, 1081
—, 2004, A&A, 428, 1001
Collier Cameron A. et al., 2006, MNRAS, 373, 799
—, 2007, MNRAS, 380, 1230
Cowan N. B., Agol E., 2011, ApJ, 726, 82
Demarque P., Woo J.-H., Kim Y.-C., Yi S. K., 2004, ApJS, 155, 667
Ehrenreich D., Désert J., 2011, arXiv:1103.0011
Enoch B. et al., 2011, MNRAS, 410, 1631
Enoch B., Collier Cameron A., Parley N. R., Hebb L., 2010, A&A, 516, A33
Faedi F. et al., 2011a, arXiv:1102.1375
Faedi F., West R. G., Burleigh M. R., Goad M. R., Hebb L., 2011b, in American Institute of Physics Conference Series, Vol. 1331, American Institute of Physics Confer-

ence Series, S. Schuh, H. Drechsel, & U. Heber, ed., pp. 254–261

Fortney J. J., Marley M. S., Barnes J. W., 2007, ApJ, 659, 1661

Gillon M. et al., 2009, A&A, 501, 785

Gillon M., Jehin E., Magain P., Chantry V., Hutsemékers D., Manfroid J., Queloz D., Udry S., 2011, Detection and Dynamics of Transiting Exoplanets, St. Michel l'Observatoire, France, Edited by F. Bouchy; R. Díaz; C. Moutou; EPJ Web of Conferences, Volume 11, id.06002, 11, 6002

Goldreich P., Soter S., 1966, Icarus, 5, 375

Hansen B. M. S., 2010, ApJ, 723, 285

Hellier C. et al., 2011, Detection and Dynamics of Transiting Exoplanets, St. Michel l'Observatoire, France, Edited by F. Bouchy; R. Díaz; C. Moutou; EPJ Web of Conferences, Volume 11, id.01004, 11, 1004

—, 2010, ApJ, 723, L60

Ibgui L., Spiegel D. S., Burrows A., 2011, ApJ, 727, 75

Laughlin G., Marcy G. W., Vogt S. S., Fischer D. A., Butler R. P., 2005, ApJ, 629, L121

Lucy L. B., Sweeney M. A., 1971, AJ, 76, 544

Magain P., 1984, A&A, 134, 189

Mandel K., Agol E., 2002, ApJ, 580, L171

Maxted P. F. L. et al., 2010, arXiv:1012.2977

Pepe F. et al., 2005, The Messenger, 120, 22

Pollacco D. et al., 2008, MNRAS, 385, 1576

Pollacco D. L. et al., 2006, PASP, 118, 1407

Pont F., Husnoo N., Mazeh T., Fabrycky D., 2011, MNRAS, 378

Queloz D. et al., 2010, A&A, 517, L1+

—, 2001, A&A, 379, 279

—, 2000, A&A, 354, 99

Schlaufman K. C., 2010, ApJ, 719, 602

Seager S., Mallén-Ornelas G., 2003, ApJ, 585, 1038

Sestito P., Randich S., 2005, A&A, 442, 615

Simpson E. K. et al., 2010, arXiv:1011.5664

Skrutskie M. F. et al., 2006, AJ, 131, 1163

Stetson P. B., 1987, PASP, 99, 191

Torres G., Andersen J., Giménez A., 2010, A&A Rev., 18, 67